Hindawi
Advances in Civil Engineering
Volume 2024, Article ID 6698625, 18 pages
https://doi.org/10.1155/2024/6698625

Research Article

Large Ring Test for Evaluation of Restrained Shrinkage Cracking: Calibration and Experimental Trial

Zhongyu Xu,[1] **Lucija Hanžič**,[2] **Harry Asche**,[1,3] **and Jurij Karlovšek**[1]

[1]*School of Civil Engineering, The University of Queensland, Building 49 Staff House Road, Street Lucia, Brisbane, QLD, Australia*
[2]*Slovenian National Building and Civil Engineering Institute (ZAG), Dimičeva ulica 12, 1000 Ljubljana, EU, Slovenia*
[3]*Aurecon, 25 King Street, Bowen Hills, QLD, Australia*

Correspondence should be addressed to Zhongyu Xu; zhongyu.xu@uq.edu.au

Received 15 June 2023; Revised 5 March 2024; Accepted 14 March 2024; Published 5 April 2024

Academic Editor: Payam Shafigh

The durability of shotcrete tunnel linings is significantly affected by restrained shrinkage cracking. Given the unique characteristics of shotcrete applied in tunnel linings, especially when dealing with accelerated shotcrete containing reinforcement fibres, it is necessary to upscale the ring test commonly used. This paper presents a comprehensive experiment using large ring tests with cast concrete to investigate the impact of upscaling ring test geometry. The two ring specimens demonstrated comparable cracking age (22 days) and strain measured in the steel ring, suggesting that consistent results can be obtained through the proposed instrumentation, calibration, and correction methods. Moreover, the estimated induced tensile stresses of the concrete rings (2.8 and 2.7 MPa) are slightly lower than the predicted tensile strength (3.3 MPa) at the age of cracking, which indicates that some driving forces contributing to restrained shrinkage cracking were not indicated in the strain gauge readings. Furthermore, the study identified multi-crack formation and additional potential causes for crack initiation, which include self-restraint due to the moisture gradient in the vertical direction, deflection of the concrete ring caused by its self-weight, and friction on the contact surface of the support. Therefore, optimising the geometry of the ring specimens and the apparatus is imperative to minimise additional driving forces and unmeasurable restraints for crack initiation, especially when employing the stress rate method to assess cracking potential.

1. Introduction

The demand for tunnelling and underground construction is steadily increasing. In Australia, the annual expenditure on rail and road infrastructure for 2022/23 is approximately 20 billion AUD [1], with tunnelling playing a crucial role in nearly half of these projects. Among the upcoming projects scheduled to commence in 2022/23 are the *North-East Link and Suburban Rail Loop* in Victoria [2, 3], *the Western Harbour Tunnel and Coffs Harbour Bypass in* New South Wales [4, 5] and *the Inland Rail* in Queensland [6]. Sprayed concrete, commonly known as shotcrete, plays a significant role in many tunnel projects, serving both temporary and permanent ground support purposes [7, pp. 1:5–1:6]. With the escalating demand for tunnelling, the quality of shotcrete is receiving heightened attention and has become a focal point for research on its behaviour, durability, and sustainability.

In comparison to ordinary cast concrete, shotcrete applications in tunnelling for ground support exhibit several significant differences, including:

(i) Shotcrete mixes have a higher proportion of cement and sand, incorporating smaller-grain aggregates to achieve suitable pumpability and sprayability [7, pp. 7:1–7:5]. The rebound during application results in the loss of coarse aggregates, leading to a lower proportion of coarse aggregate and a relatively higher cement content in the sprayed shotcrete.

(ii) Shotcrete is applied to the substrate at high velocity and is compacted purely by momentum upon impact.

(iii) Shotcrete setting and hardening are accelerated with chemical admixtures to ensure adherence to the substrate without sagging and to allow for safe re-entry into the tunnel as quickly as possible.

(iv) Shotcrete is subjected to loading almost immediately after spraying.

(v) Shotcrete is applied in relatively thin layers, resulting in a large, exposed surface-to-volume ratio. Consequently, significant water loss occurs either through evaporation on the free surface or absorption by the substrate on the adhesive surface. The challenging tunnel environment further complicates proper concrete curing due to the difficulty in maintaining moisture.

Furthermore, there is a strong preference, driven by safety and cost considerations, to avoid using bar and mesh reinforcement in shotcrete for ground support. Consequently, shotcrete used in Australian tunnels often incorporates steel fibres for reinforcement [7, pp. 7:1–7:7].

It has been determined that the shrinkage of shotcrete employed for tunnel linings is considerably greater than that of standard cast concrete [8]. This increased shrinkage can be attributed to unique features of the shotcrete used in tunnel linings, encompassing set accelerators, rebound, spraying techniques, composition, a large exposed surface-to-volume ratio, and curing environments [9–11]. It is noteworthy that shrinkage in shotcrete utilised as ground support can be deemed beneficial if the ground is moving inward in response to advancing excavation. This effect was acknowledged by the early advocates of shotcrete as ground support [12]. However, in shallow tunnels in hard rock, such as those commonly found in Sydney, shotcrete shrinkage can pose challenges because it may induce tension in the lining, particularly in long-term permanent linings [13–15].

Neville [16, pp. 423–428] distinguishes among three types of shrinkage occurring in concrete after casting: plastic, autogenous, and drying shrinkage. Plastic shrinkage arises from water suction by the underlying rock or soil or water evaporation from the surface while the concrete is still in a plastic state [16, p. 424]. Autogenous shrinkage results from a difference in the volume occupied by hydration products compared to the volume occupied by reagents (cement and water) [16, p. 426]. Under sealed conditions, this difference amounts to 6–8 vol% [16, pp. 26–31, 17]. The mechanisms of autogenous shrinkage are extensively discussed by Tazawa [18]. In terms of linear strain, volume changes due to autogenous shrinkage within the first month of hydration amount to approximately 40 $\mu\varepsilon$ in normal-strength concrete [16, p. 425]. On the other hand, drying shrinkage results in a significantly higher linear strain, with observed values reaching up to 4,000 $\mu\varepsilon$ [16, p. 426]. Drying shrinkage mechanisms, namely capillary and surface tension, movement of interlayer water, and disjoining pressure, are explained in detail by Ye and Radlińska [19].

In predicting shrinkage, factors such as the type of concrete (normal vs. high strength), its constituents (ordinary Portland vs. composite cement), volume fractions of constituents, and the type and geometry of the concrete structure must be considered. Often, one or two types of shrinkage dominate, rendering other types negligible. For instance, the structural design standard Eurocode 2 [20, 21] only incorporates autogenous and drying shrinkage. In the context of shotcrete tunnel linings, the use of accelerators causes the concrete to rapidly set upon surface impact, making plastic shrinkage of secondary importance in the shotcrete used for tunnel linings. Additionally, the shotcrete lining, being a thin structure with a high surface area-to-volume ratio, facilitates water loss through evaporation, making drying shrinkage the most significant of the three types of shrinkage [22]. As recommended by Ye and Radlińska [19], in normal-strength concrete, autogenous shrinkage represents an insignificant part of total shrinkage. Therefore, there is no need to differentiate it from drying shrinkage. This assumption applies to shotcrete tunnel linings in Australia, considering the typical 28-day unconfined compressive strength (UCS) of shotcrete used in Australia ranges between 40 and 50 MPa [7, p. 5:2]. Consequently, this paper focuses on drying shrinkage; however, the measured values include autogenous shrinkage as well.

The impact of drying shrinkage is even more pronounced in accelerated shotcrete used in tunnel constructions. Part of the increased shrinkage is because using accelerators leads to the hydration reaction taking place in stiff material, resulting in coarser porosity, and the resultant coarser porosity contributes to an increase in drying shrinkage [9]. The cracks that form in young concrete severely impact the durability of shotcrete linings as they prompt the development of large cracks due to strain softening [15]. In addition to shrinkage during the stiffening and hardening stage, shrinkage can also occur in mature concrete due to thermal changes, carbonation, and phase transitions. However, these causes fall outside the scope of this paper.

If shrinkage is constrained by substrates like rock or a layer of mature concrete, internal stress is generated, leading to fracture and cracking [23]. The cracking potential of concrete is influenced not only by the free shrinkage of the concrete mix (namely the potential for volumetric changes) but also by other time-dependent factors such as stress development under a specific degree of restraint (DOR), strength gain over time, stress relaxation, and fracture toughness [24, 25]. Therefore, the Australian tunnelling industry has recognised the need for a test method other than free drying shrinkage assessment, such as AS1012.13 [26]. A method that considers restrained shrinkage of plain or fibre-reinforced shotcrete (FRS) is thus a goal for the tunnelling industry.

The assessment of restrained shrinkage can be undertaken with various setups. Carlswärd [27] compared end-restrained, base-restrained, and ring tests to evaluate cracking caused by shrinkage under restrained conditions. Although the uniaxial restrained shrinkage tests with either end or base restraints show simplicity for stress evaluation, the additional analysis for deformable restraints or the inconsistency of the bond condition of the restraint makes them less favourable. In-ring tests, a concentric steel ring acts as the restraint, and the deformation of the restraint (steel ring) is measured and utilised for the analysis. Additionally, Noghabai [28] explains the analogy between cracking in a thick-walled cylinder with internal pressure and cracking in a plate with uniaxial tension.

Standardised ring tests, such as ASTM C1581 [29] and AASHTO T334 [30], use apparatuses with a concrete ring thickness of 37.5 and 76 mm, respectively, for the quantitative evaluation of the cracking potential of concrete under

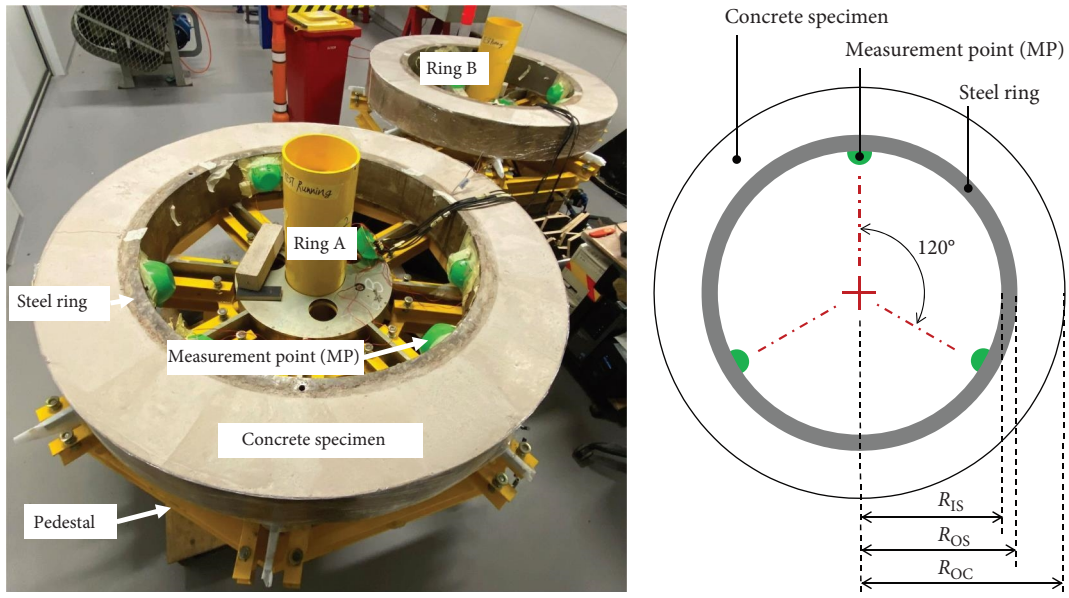

FIGURE 1: The large ring setup for the restrained shrinkage test comprises a pedestal and a steel ring, illustrated in (a). Three measurement points (MP) are strategically positioned on the inner circumference of the steel ring, as depicted schematically in (b). Here, R_{IS}, R_{OS}, and R_{OC} represent the inner radius, outer radius of the steel ring, and outer radius of the concrete ring, respectively.

restrained shrinkage. However, Raoufi et al. [31] concluded that the restrained shrinkage cracking behaviour of reinforced concrete is size-dependent due to damage localisation, and smaller rings tend to exhibit smaller crack widths at a given age than observed in larger rings. Specifically, specimens like slabs in the field (generally 3,000–6,000 mm long) experience larger crack openings compared to smaller specimens like the ASTM C1581 [29] concrete ring, which corresponds to a slab of about 1,000 mm long [31]. The size dependency implies that the relatively small size of the restrained ring test may overestimate the performance of fibre-reinforced concrete when compared with the performance of these mixtures in the field.

Furthermore, mould size and geometry are key considerations for selecting test methods for FRS. In FRS, the distribution and orientation of the fibres influence mechanical performance, especially crack-bridging and energy absorption [32]. Several studies have explored fibre orientation in cementitious materials and how it is impacted by mould size and geometry (wall effect) [33, 34]. It is concluded that the reinforcement fibres tend to be oriented parallel to the walls and/or surface of the framework [33], and the orientation of fibres in FRS depends on the spraying techniques as well as the size and geometry of the sampling mould [35]. Therefore, standardised tests for FRS favour specimens produced by spraying concrete into large moulds, reducing defects and inconsistencies caused by limited spraying angles, rebound, and inadequate compaction, leading to lower variation in results [36, 37].

In past studies, the production of shotcrete ring specimens with standardised ring moulds has been achieved by spraying shotcrete without fibres [38, 39]. However, the length of macro steel fibres used in shotcrete tunnelling linings is between 30 and 35 mm [40], while macro-synthetic fibres range from 45 to 65 mm [41, 42]. Spraying FRS at high velocity into a mould with a width less than three times the fibre length may force a significant portion of the fibres in the ring specimen to align in the circumferential direction, which is not representative of the distribution in actual FRS applications.

Implementing a restrained shrinkage test to assess shotcrete used for tunnel lining calls for a larger test setup, especially when studying FRS. However, scaling up is not a straightforward process because size effects are not negligible in geometrically similar structures of different sizes. Bazant and Planas [43, pp. 9–11] explain various sources of size effects, including boundary layer effects, diffusion phenomena, and fracture mechanics size effects, which are intrinsic features of testing and sampling. The review conducted by Kanavaris et al. [44] on ring tests for restrained shrinkage of concrete shows no publications on this topic with specimen height >160 mm and concrete ring thickness >80 mm.

The aim of this study is to adopt an upscaled ring test to assess the restrained shrinkage of cast concrete and identify aspects for improvement. The motivation for studying the restrained shrinkage of shotcrete was triggered by the Australian tunnelling industry and its interest in systematically addressing the cracking of shotcrete in tunnel linings. The findings from this experimental trial can be helpful for optimising the large ring test method and making it more suitable for testing sprayed fibre-reinforced concrete in future work.

2. Methods

The study introduces the large, restrained shrinkage ring setup, illustrated in Figure 1(a), consisting of a steel ring and pedestal. The steel ring has an outer radius (R_{OS}) of 600 mm and a wall thickness of 55 mm, results in an inner

Table 1: Comparison between the ASTM C1581 (2009), AASHTO T334 (2008), and upscaled ring used in this study.

Parameter			ASTM C1581	AASHTO T334	Upscaled ring
Inner radius of the steel ring		R_{IS} (mm)	152.5	140.0	545
Outer radius of the steel ring		R_{OS} (mm)	165.0	152.5	600
Outer radius of the concrete ring		R_{OC} (mm)	202.5	228.5	800
Height of concrete and steel ring		h (mm)	150	152	200
Drying direction			Circumferential	Circumferential	Radial
R_{OS} to R_{OC} ratio		R_{OC}/R_{OS} (m m^{-1})	1.23	1.50	1.33
Exposed surface-to-volume ratio		S_{exp}/V (m^2 m^{-3})	29	16	10
Degree of restraint—see Equation (1)		DOR (%)	80	70	78
Hoop strain on steel as per Equation (2)	If $\varepsilon_{C-sh} = 300\,\mu\varepsilon$	ε_S ($\mu\varepsilon$)	70	100	75
	If $\varepsilon_{C-sh} = 1{,}000\,\mu\varepsilon$		225	335	250

radius (R_{IS}) of 545 mm. The base part of the formwork comprises the pedestal support and plywood sections. Once the concrete hardens, the plywood sections can be removed, exposing the bottom surface to drying conditions.

Three measurement points (MPs) are positioned on the inner circumference of the steel ring, each separated by a 120° angle. Casting the concrete around the steel ring is facilitated by a metal strip, constituting the outer part of the formwork. This strip is placed on the pedestal and securely fixed concentrically to the steel ring using spacers. The outer radius of the concrete ring (R_{OC}) is 800 mm, resulting in a concrete ring thickness of 200 mm. Both the steel and concrete rings have a height (h) of 200 mm. To ensure consistent quality and eliminate defects caused by spray techniques and rebound, cast concrete is utilised instead of sprayed concrete. The subsequent sections delve into the implications of ring geometry, instrumentation, and calibration.

2.1. Implications of Ring Geometry. Unlike the drying shrinkage test, which determines the response of concrete to standard drying conditions, the restrained ring test involves interactions between the test material (the concrete/shotcrete ring) and the steel ring. The impact of ring geometry can be assessed by considering the DOR [45]. For instance, when assessing thin structures fully bonded to the substrate, a high DOR setup should be employed. In contrast, evaluating bulk structures restrained only at either end requires a low DOR. However, a trade-off with strain measurements must be considered; a high DOR results in a smaller strain measured on the steel ring, reducing the sensitivity of the system.

Ring geometry also encompasses the surfaces through which drying takes place, whether circumferential or radial, involving either the external perimeter or the top and bottom surfaces of the concrete ring. In the case of circumferential drying, the outer surface of the concrete ring dries more rapidly than the inner surface, leading to differential shrinkage. Consequently, the self-restraining effect is induced, peaking on the outer perimeter—opposite to the restraining effect induced by the steel ring, which peaks on the inner circumference of the concrete ring [46]. In contrast, radial drying results in uniform drying of concrete on the inner and outer perimeters without inducing additional restraining effects.

Analytically, DOR for radial drying, according to Moon [45, pp. 44–48], is given as follows:

$$\mathrm{DOR} = 1 - \frac{1}{2} \cdot \frac{\varepsilon_S(t)}{\varepsilon_{C-sh}(t)} \cdot \left(\left(\frac{R_{IS}}{R_{OS}} \right)^2 (1 + \upsilon_S) + (1 - \upsilon_S) \right), \tag{1}$$

where

$$\frac{\varepsilon_S(t)}{\varepsilon_{C-sh}(t)} = \frac{\frac{E'_C}{E_S} \cdot \frac{2}{1 - \left(\frac{R_{IS}}{R_{OS}} \right)^2}}{\frac{E'_C}{E_S} \cdot \frac{(1+\upsilon_S)\left(\frac{R_{IS}}{R_{OS}} \right)^2 + (1-\upsilon_S)}{1 - \left(\frac{R_{IS}}{R_{OS}} \right)^2} - \frac{(1+\upsilon_C)\left(\frac{R_{OC}}{R_{OS}} \right)^2 + (1-\upsilon_C)}{1 - \left(\frac{R_{OC}}{R_{OS}} \right)^2}}. \tag{2}$$

The time-dependent variables ε_S and ε_{C-sh} (m m^{-1}), representing the strain on the inner surface of the steel ring in the hoop direction and the linear free shrinkage of concrete, respectively, are functions of time t(s). Additionally, E_S (200 GPa) and ν_S (0.3) denote the elastic modulus and Poisson's ratio of steel, while E_C (∼21 GPa) and ν_C (∼0.18) denote the time-dependent effective elastic modulus and Poisson's ratio of concrete.

Simulations conducted by Moon [45, pp. 52–62] indicate that, to a reasonable extent, DOR is independent of moisture conditions inside the concrete. Consequently, Equations (1) and (2) can be adapted for circumferential drying as well. Furthermore, the parametric study reveals that ν_C in the range between 0.15–0.25 has an insignificant impact on the DOR, while the effect of E_C in the range between 15 and 25 GPa is less than 10%. Thus, the values employed by Moon [45], as mentioned above, can be utilised to estimate DOR values. Moreover, Equation (2) can be employed to estimate the expected range of ε_S, which is crucial for selecting instrumentation for strain acquisition, assuming the values of ε_{C-sh} are anticipated in the range between 300 and 1,000 $\mu\varepsilon$. A summary of the comparison between ASTM C1581 ring [29] and AASHTO T334 [30] rings and the upscaled ring used in this study is provided in Table 1.

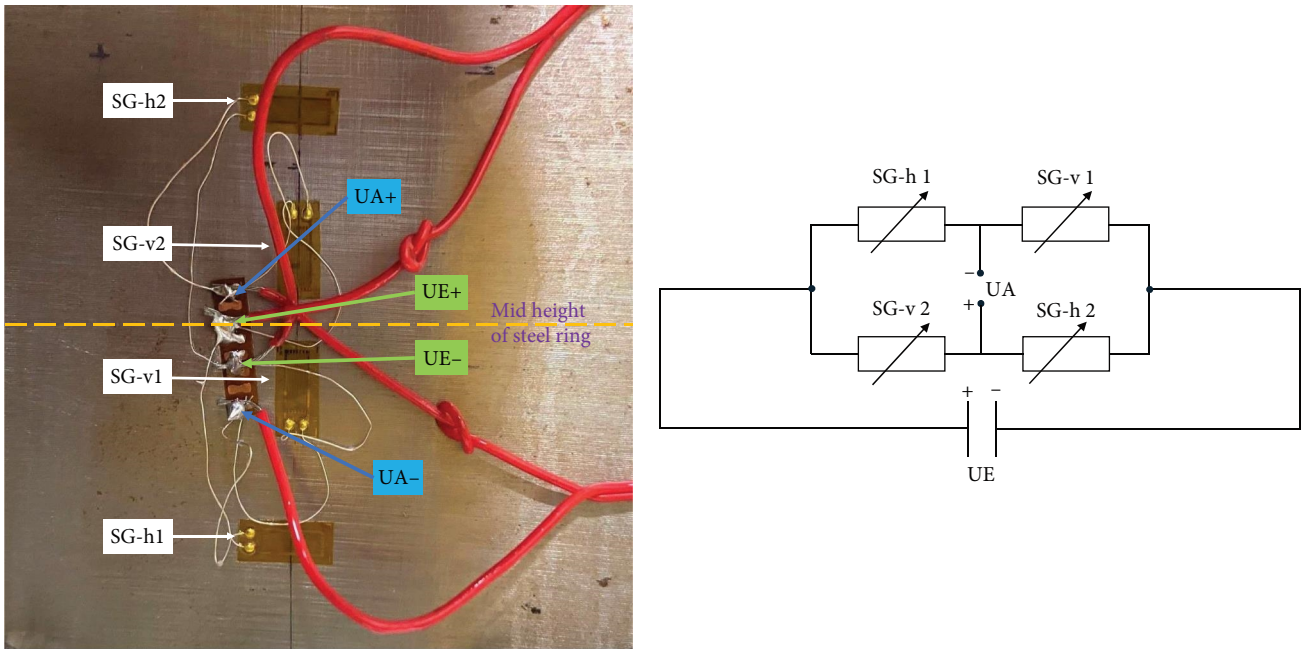

FIGURE 2: The full wheatstone bridge adapted for strain measurements on the inner surface of the steel ring is depicted, illustrating (a) the configuration of strain gauges and (b) the schematic circuit diagram. Strain gauges (SG) labelled h1 and h2 are affixed in the hoop direction, while v1 and v2 are attached in the vertical direction. U_E denotes the excitation voltage, and U_A is the output voltage of the bridge. The centreline at half-height of the steel ring passes between v1 and v2.

The comparison of R_{OC} to R_{OS} ratio and DOR values reveals that the upscaled ring test is designed with geometrical similarity to standardised ring tests. It possesses a DOR value of 78%, comparable to the ASTM C1581 [29] ring with 80% and slightly higher than that of AASHTO T334 [30] with 70%. These values are considered high, given that the DOR can range from approximately 10% to 95%. A high DOR is particularly necessary in the case of tunnel linings, where the concrete layer is thin and considered fully bonded to the underlying surface. The implications of the DOR were thoroughly studied by Raufi et al. [31].

The ratio between the surface exposed to drying S_{exp} (m^2) and the volume V (m^3) of the specimen or structure influences the drying rate and, consequently, the drying shrinkage. A larger exposed surface-to-volume ratio (S_{exp}/V ratio) implies that moisture needs to travel a shorter distance from the core to the surface. As presented in Table 1, upscaling the ring at approximately the same DOR and changing the drying direction from circumferential to radial resulted in a threefold reduction in the S_{exp}/V ratio compared to ASTM and a 1.5-fold decrease compared to AASHTO. Consequently, the drying rate in the upscaled ring is reduced, leading to a longer time to cracking.

2.2. Instrumentation. For strain measurements in ring tests, electrical resistance strain gauges are commonly utilised on the inner circumference of the steel ring. However, the detailed arrangement of strain gauge circuits is not extensively discussed in publications. Some authors have opted for a half-bridge configuration for temperature compensation [47–51], while a full Wheatstone bridge is also recommended [52]. The large ring test is expected to have a prolonged test duration due to a smaller S_{exp}/V ratio, which affects not only drying but also heat dissipation. Furthermore, the heat released during the hydration of a larger volume of concrete cannot be considered negligible. Thus, in this study, strain gauges are organised in a full Wheatstone bridge configuration to minimise adverse effects from temperature changes, noise, manufacturing tolerance, alignment errors, and additional resistance from lead wires, particularly for tests lasting weeks.

Three MPs are positioned on the inner circumference of the steel ring at 120° angles, as illustrated in Figure 1(b). Each MP comprises four 5 mm long strain gauges with 120 Ω resistance arranged in a full Wheatstone bridge, as presented in Figure 2(b). Circumferential strain is measured with two strain gauges aligned in the hoop direction, labelled SG-h, while two vertical strain gauges, labelled SG-v, serve for temperature compensation to counteract the thermal expansion of the steel rings. As the test is conducted in a temperature-controlled room, the primary source of thermal expansion for the steel ring is the hydration heat, especially considering the relatively small surface-to-volume ratio of the concrete specimen with respect to heat dissipation. Consequently, the temperature of the steel ring is monitored by a thermocouple attached to it. The output of the Wheatstone bridge and thermocouples is recorded by the data logger, specifically the *dataTaker DT800*, at a frequency of 1 record every 5 s.

The strain measured by the Wheatstone bridge is related to voltage changes as follows [53]:

$$\frac{U_A}{U_E} = \frac{1}{4}\left(\frac{\Delta R_1}{R_1} - \frac{\Delta R_2}{R_2} + \frac{\Delta R_3}{R_3} - \frac{\Delta R_4}{R_4}\right) = \frac{k}{4}(\varepsilon_1 - \varepsilon_2 + \varepsilon_3 - \varepsilon_4). \tag{3}$$

In the given equation, U_A (V) represents the bridge output voltage, U_E (V) denotes the excitation voltage, k (unitless) is the strain-gauge factor (2.16), R_1 to R_4 represent the electrical resistance of the four active strain gauges in the Wheatstone bridge. Additionally, ΔR_1 to ΔR_4 indicate changes in resistance, while ε_1 to ε_4 denote the strain experienced by the strain gauges under deformation. It is assumed that temperature strain (ε_T) is uniform in all directions:

$$R_1 = \mathrm{SG}_{v1}, \qquad \varepsilon_1 = \varepsilon_T + \varepsilon_{v1}, \tag{4}$$

$$R_2 = \mathrm{SG}_{h1}, \qquad \varepsilon_2 = \varepsilon_T + \varepsilon_{h1}, \tag{5}$$

$$R_3 = \mathrm{SG}_{v2}, \qquad \varepsilon_3 = \varepsilon_T + \varepsilon_{v1}, \tag{6}$$

$$R_4 = \mathrm{SG}_{h2}, \qquad \varepsilon_4 = \varepsilon_T + \varepsilon_{h2}. \tag{7}$$

The mechanical strains, ε_{h1}, ε_{h2}, and ε_{v1}, ε_{v2} (m m^{-1}), result from external forces in either the hoop (h) or vertical (v) directions at positions 1 (lower) and 2 (upper). While Moon [45] suggests that the influence of moisture gradient along the height direction on DOR is reasonably insignificant, it is important to note that the highest pressure applied on the steel ring occurs in the middle of the height. As drying progresses, the pressure tends to approach a more uniform distribution along the height [45]. Therefore, to ensure comparable readings for hoop strain from the two strain gauges at each MP, they are not installed at the mid-height but rather 15 mm away from the mid-height and symmetric about the mid-height line (refer to Figure 2(a)).

Consequently, Equation (3) can be expressed with temperature strain and mechanical strains as follows:

$$\frac{U_A}{U_E} = \frac{k}{4}[(\varepsilon_T + \varepsilon_{v1}) - (\varepsilon_T + \varepsilon_{h1}) + (\varepsilon_T + \varepsilon_{v2}) - (\varepsilon_T + \varepsilon_{h2})]. \tag{8}$$

Given that the strain gauge placement is symmetric to the mid-height of the steel ring and assuming equal drying conditions on the top and bottom surfaces, the deformation of the steel ring caused by concrete shrinkage in positions 1 and 2 is considered identical ($\varepsilon_{h1} = \varepsilon_{h2}$ and $\varepsilon_{v1} = \varepsilon_{v2}$). Hence, Equation (3) is simplified to the following:

$$\frac{U_A}{U_E} = \frac{k}{2}(\varepsilon_h - \varepsilon_v). \tag{9}$$

As $\varepsilon_v = -\nu_S \cdot \varepsilon_h$, the hoop strain can be estimated with the voltage output, Poisson's ratio, and gauge factor:

$$\varepsilon_h = \frac{2}{k(1+\nu_s)} \cdot \frac{U_A}{U_E}. \tag{10}$$

The use of a full Wheatstone bridge configuration for strain gauge arrangement supplemented with thermocouples for temperature monitoring is also suitable for specimens made of sprayed shotcrete. For the shotcrete applications in tunnelling, where set accelerators are added to the shotcrete for overhead placement to achieve high early-age strength for re-entry time, the fast release of heat due to the accelerator reaction is substantial. The combination of a full Wheatstone bridge and thermocouples ensures that the evaluation accounts for the temperature effects. The number of MPs can be increased to capture the local strain changes during cracking.

2.3. Calibration of the Instrumented Ring. Calibration is a crucial step preceding restrained shrinkage tests to ensure precision in data acquisition. Swamy et al. [54] estimated the elastic modulus of the steel ring by applying compression across its diameter. However, their approach solely utilised deflection to determine the elastic modulus without providing readings from individual strain gauges. In contrast, Zieliński and Kaszyńska [55] proposed an innovative calibration method for the steel ring, employing a pressurised inflatable rubber collar on the outer circumference. Nevertheless, due to equipment availability, Swamy's cross-diameter compression method was adopted. This method also offers flexibility for calibrating steel rings of various sizes with a straightforward and easily adjustable setup.

In the calibration process, a compressive force was applied perpendicularly onto the outer wall of the ring, acting across the diameter, with the opposite side of the ring resting against the reaction wall, as depicted in Figure 3. The load P (in Newtons) was incrementally applied in 4 kN steps, ranging from 0 to 16 kN, using a hydraulic jack. The ring was positioned to have one MP directly on the line of action (Loc 1), while the other two (Locs 2 and 3) were symmetrically located on either side of the line of action, forming a 60° angle. The test was repeated three times, and between each repetition, the ring was rotated by 120°, ensuring that each MP assumed all three locations.

To validate the strain measurements on the inner circumference of the steel ring, a comparison was made with strain values calculated using an analytical solution for a thin ring subjected to two opposite compressive forces, P, acting across the diameter [56]. In the case of a curved beam, where the depth of the cross-section is small compared to the radius, the distance to the neutral axis from the centroid of the cross-section can be neglected when calculating the bending moment [56]. In this specific scenario, the steel ring's depth and radius are 55 and 545 mm, respectively. Therefore, it is assumed that the neutral axis passes through the centroid of the cross-section in this geometrically thin ring. This solution is considered appropriate since the thickness of the steel ring is 10% of its inner radius. The circumferential strain at a distance y from the neutral surface is expressed as follows [56]:

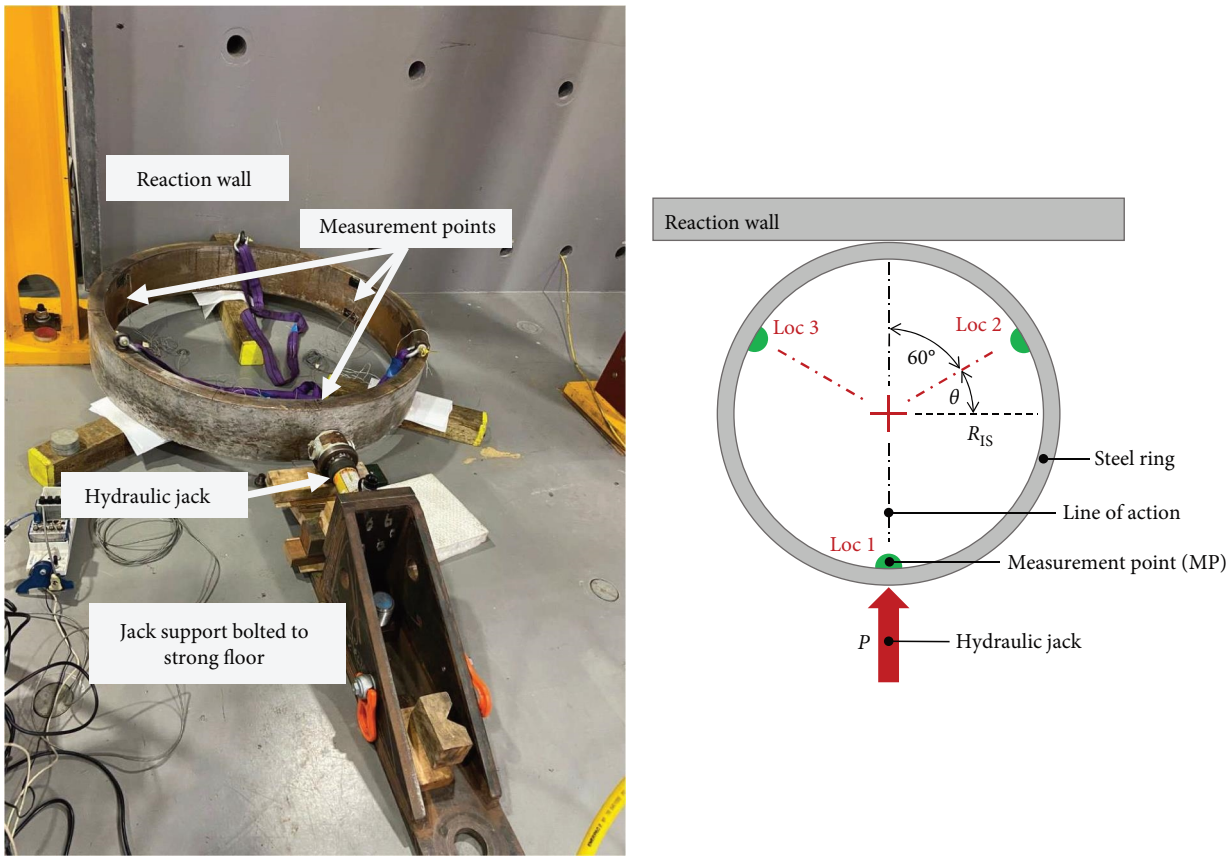

(a) (b)

FIGURE 3: The calibration setup of the steel ring is illustrated with (a) a photograph of the setup and (b) a graphical presentation where P (in Newtons) is the point load applied by the hydraulic jack, R_{IS} (m) is the inner radius of the steel ring, and θ (in degrees) is the angle measured from the line perpendicular to the line of action passing through the centre of the ring, where no displacement occurs in the direction of the line of action.

$$\varepsilon = \frac{y\mathrm{MR}}{(R_n - y)E_S I}, \tag{11}$$

where y represents the distance to the neutral surface, defined as half of the thickness of the steel ring (27.5 mm) measured from the inner circumference, R_n is the radius of the neutral surface, which corresponds to the distance from the ring centre to the mid-thickness of the steel ring (572.5 mm), and I denotes the moment of inertia, calculated as $2.77 \times 10^{-6}\,\mathrm{m}^4$ for a cross-section measuring 55 mm × 200 mm. The bending moment of the cross-section in a thin ring at an angle under two opposite compressive forces acting across the diameter can be derived using the Castigliano theorem [56, 57]:

$$M = \frac{\mathrm{PR}}{2}\left[\frac{2}{\pi} - \cos(90° - \theta)\right], \tag{12}$$

where R (m) represents the radius ranging from R_{IS} to R_{os}, θ (deg) is the angle between the line of action and the MP (see Figure 3). Due to the symmetry of the ring, θ values range from 0° to 90°, with $\theta = 90°$ for Loc 1 and $\theta = 60°$ for Locs 2 and 3.

The calculated bending moment can be used to estimate the circumferential strain on the inner surface of the steel ring. Using Equations (11) and (12), the strain in the hoop direction at Loc 1 is estimated at 152 $\mu\varepsilon$, while at Locs 2 and 3, the estimated value amounts to −55 $\mu\varepsilon$, assuming an elastic modulus of 200 GPa and a compressive force of 16 kN. The measured strain values at the maximum and second maximum loads (12 and 16 kN) are provided in Table 2.

The measured values exhibit slight differences from the estimated values obtained by the analytical solution using $E_S = 200$ GPa, and this difference may arise from the uncertainty of the elastic modulus. Additionally, due to the curvature of the ring and the thickness being 10% of the radius, the approximation of the actual neutral surface may contribute to a discrepancy between the estimated and measured values. Finite element (FE) simulation was conducted in ANSYS Mechanical APDL with the same dimensions and loading conditions, assuming an elastic modulus of 200 GPa and a Poisson's ratio of 0.3. The FE results align closely with the analytical results, showing 144 $\mu\varepsilon$ in the circumferential direction and 53 $\mu\varepsilon$ in the vertical direction at $\theta = 0°$. Thus, the effective elastic modulus (E_S) can be estimated by using the analytical solution with the measured steel ring strains (as shown in Table 3).

Table 2: Results of calibration test on Rings A and B showing strain measured at point load $P = 12$ and 16 kN applied at Loc 1 (see Figure 3).

Ring	Strain gauge in Loc 1	Applied force (kN)	Strain ($\mu\varepsilon$)			Elastic modulus (GPa)		
			MP1	MP2	MP3	MP1	MP2	MP3
A	MP1	12	88	−39	−33	258	210	249
		16	119	−50	−44	255	219	249
	MP2	12	−32	88	−37	256	258	222
		16	−44	118	−49	249	257	223
	MP3	12	−34	−35	93.8	241	235	243
		16	−49	−49	127	223	223	239
B	MP1	12	94	−38	−35	242	216	235
		16	125	−52	−47	243	210	233
	Mid MP1–MP2	12	−39	−37	89	210	222	256
		16	−52	−50	121	211	219	251
	MP2	12	−35	96	−40	235	237	205
		16	−48	128	−53	228	237	027
	Mid MP2–MP3	12	84	−41	−35	271	200	235
		16	114	−55	−45	266	199	243
	MP3	12	−36	−33	92	228	249	248
		16	−48	−46	122	228	238	249
	Mid MP1–MP3	12	−37	89	−38	222	256	216
		16	−49	119	−51	223	255	215

MP stands for the measurement point, which is a full Wheatstone bridge shown in Figure 2.

Table 3: Effective elastic moduli (E_S') and the average effective modulus $\overline{E}_S$ for Ring A and Ring B.

Ring	Effective elastic modulus $E_{S'}$ (GPa)				Calibration coefficient α		
	MP1	MP2	MP3	$\overline{E}_S$	MP1	MP2	MP3
A	247	234	237	239	1.03	0.98	0.99
B	234	228	233	232	1.01	0.98	1

Let α be the calibration coefficient, representing the ratio of the effective elastic modulus E_S (GPa) to the average elastic modulus $\overline{E}_S$ (GPa) as follows:

$$\alpha = \frac{E_S'}{\overline{E}_S'}. \tag{13}$$

Thus, the corrected elastic strain of the inner circumference of the steel ring can be obtained by applying calibration coefficient α on the measured strain from the individual strain gauge.

An FE simulation was executed with an elastic modulus of 236 GPa (averaged value of E_S for Rings A and B) and a compressive force of 16 kN applied through the diameter to validate the estimated elastic modulus. The elastic strains obtained from the FE simulation at $\theta = 0°$ are $\varepsilon_h = 122\,\mu\varepsilon$ and $\varepsilon_v = 45\,\mu\varepsilon$. To compare with the measured hoop strain from the compression test, ε_h and ε_v from the FE simulation were input into Equation (10) to calculate the output from a full Wheatstone bridge, resulting in an output hoop strain of 128 $\mu\varepsilon$, which is comparable to the measured value. Consequently, the estimated elastic modulus from the analytical method proves to be sufficiently accurate, and the calibration coefficients α can be confidently employed to correct ring test results.

It is worth noting, however, that this calibration is based on an analytical solution for geometrically thin rings. Alternative calibration methods should be considered if the steel ring is regarded as a geometrically thick ring. Moreover, the temperature compensation of the full Wheatstone bridge configuration ensures that only the mechanical strain from the strain gauges is recorded in calibration. Thus, the calibration on the instrumented steel ring with strain gauges arranged with full Wheatstone bridge configurations is less sensitive to the temperature. Nevertheless, sudden temperature changes should be avoided to minimise the effect of the significant thermal expansion of the steel ring.

3. Materials and Specimen Preparation

A ready-mix concrete with a nominal strength of 40 MPa, a maximum aggregate size of 10 mm, and a slump of 160 mm was supplied by an Australian concrete supplier [58] and utilised to cast two rings, Ring A and Ring B. The concrete mix design is detailed in Table 4. This specific mix design, tailored for wet-mix shotcrete applications, was chosen to achieve representative shrinkage in shotcrete tunnel lining.

Table 4: Mix design for concrete used in Rings A and B.

Component	Quantity for 1 m^3 of concrete
GP cement	300 kg
Fly ash	100 kg
10 mm aggregate	510 kg
Manufactured sand	500 kg
Fine sand	740 kg
Water	190 kg
Admixture	7.2 L

This is because the wet-mix method is commonly employed in underground construction, including both tunnelling and mining, in Australia due to its advantages, such as accurate mixing at batch, consistent quality, and the generation of less dust.

The formwork for concrete pouring was constructed as follows:

(i) Bottom: non-absorbent plywood panels were placed onto the pedestal between steel arms and covered with a layer of thin plastic sheet; steel arms support the concrete and steel rings after demoulding (plywood panels removal). Two layers of Teflon sheets were placed between the concrete and the steel arms, as Teflon–Teflon contact has a low friction coefficient [59].

(ii) Inner rim: steel ring whose outer perimeter was cladded in Teflon sheet to reduce friction.

(iii) Outer rim: a 0.75 mm thick strip of galvanised steel was bent into a circle with a radius of 800 mm and positioned onto the pedestal concentrically around the steel ring. It was affixed to the formwork bottom and held in place by several spacers.

Extreme care was taken to prevent eccentricity between the steel and the concrete ring, which would result in stress concentration on the thinner side [60] and violate the constant wall thickness requirement [19]. The concrete was poured into the formwork and compacted with poker vibrators. The top of the concrete was screeded to produce a smooth surface and then covered with an impermeable plastic sheet. Two rings, A and B, were made simultaneously from one concrete batch. The rings were placed in a temperature-controlled room at $20 \pm 1°C$ and at a relative humidity of ~70%. The strain data were acquired at 5-s intervals. The outer formwork rim and bottom plywood panels were removed 24 hr after completion of the casting, thus exposing the top and bottom surfaces to radial drying. The outer lateral surface was immediately sealed with a coating of petroleum jelly and a sheet of soft plastic to prevent circumferential drying.

Along with the rings, the specimens were cast for the following concrete characterisation tests:

(i) UCS, according to AS 1012.9 [61]: 21 cylinders with a nominal diameter of 100 mm and nominal height of 200 mm.

(ii) Modulus of elasticity and Poisson's ratio according to AS 1012.17 [62]: four cylinders with a nominal diameter of 100 mm and nominal height of 200 mm.

(iii) Splitting test according to AS 1012.10 [63]: nine cylinders with a nominal diameter of 150 mm and nominal height of 300 mm.

(iv) Modulus of rapture according to AS 1012.11 [64]: nine prisms with nominal dimensions 100 mm × 100 mm × 400 mm.

(v) Drying shrinkage according to AS 2012.13 [26]: six prisms with nominal dimensions 75 mm × 75 mm × 280 mm.

These specimens were cured either according to standard requirements or ambiently alongside the concrete rings. Testing was conducted at various time intervals in accordance with the standard methods mentioned above. The methodology for the characterisation tests is outlined in Table 5.

4. Results and Discussion

4.1. Characterisation of Concrete. The characterisation tests conducted on specimens cured under ambient conditions (similar to the ring test) revealed the following concrete properties at the age of 28 days:

(i) UCS: 39.9 ± 2.8 MPa.

(ii) Modulus of elasticity: 21.4 ± 0.7 GPa.

(iii) Poisson's ratio: 0.19 ± 0.02.

(iv) Tensile splitting strength: 3.7 ± 1.1 MPa.

(v) Modulus of rapture: 5.5 ± 0.3 MPa.

Additional specimens cured under standard conditions (with water curing) exhibited a significantly higher UCS of 51.6 ± 0.3 MPa at 28 days. The evolution of UCS for samples cured in the ambient environment over time is illustrated in Figure 4. To estimate the UCS of concrete at the time of cracking, the following empirical equation is assumed:

$$f_c(t) = a \ln(t) + b, \tag{14}$$

where f_c (t) (MPa) is UCS at time t (days) and a and b are empirical constants derived by fitting Equation (14) to test results. Using the regression method, values of a and b were calculated to be 6.3 and 19.4, respectively, with an R^2 value of 0.92. The UCS on day 22, when the rings cracked, is thus estimated at 39 MPa, approximately the same as the mean 28-day UCS. It can also predict that the tensile strength on day 22 will be similar to the 28-day tensile strength. The uniaxial tensile strength (f_t) at the age of 22 days is estimated to be 3.3 MPa from the splitting tensile strength ($f_{t,sp}$) with Equation (15) [65].

$$f_t = 0.9 f_{t,sp}. \tag{15}$$

4.2. Free Shrinkage of Concrete. Free shrinkage was measured on two sets of prisms under different curing and drying

Table 5: Methodology for characterisation tests on concrete.

Test	Specimen geometry (mm)	Standard	Number of specimens	Age at test (days)	
				Standard curing	Ambient curing
Compressive	Cylinder Φ 100 × 200	AS 1012.9 [61]	3 or 4 per age per curing	28	4, 7, 14, 21, 28
Elastic constants	Cylinder Φ 100 × 200	AS 1012.17 [62]	3 or 4 per age per curing	—	28
Tensile splitting	Cylinder Φ 150 × 300	AS 1012.10 [63]	3 or 4 per age per curing	—	7, 28
Modulus of rapture	Prism 100 × 100 × 400	AS 1012.11 [64]	3 or 4 per age per curing	—	7, 28
Drying shrinkage	Prism 75 × 75 × 280	AS 1012.13 [26]	3 per curing	0, 7, 14, 21, 28	0, 3, 6, 13, 20, 27

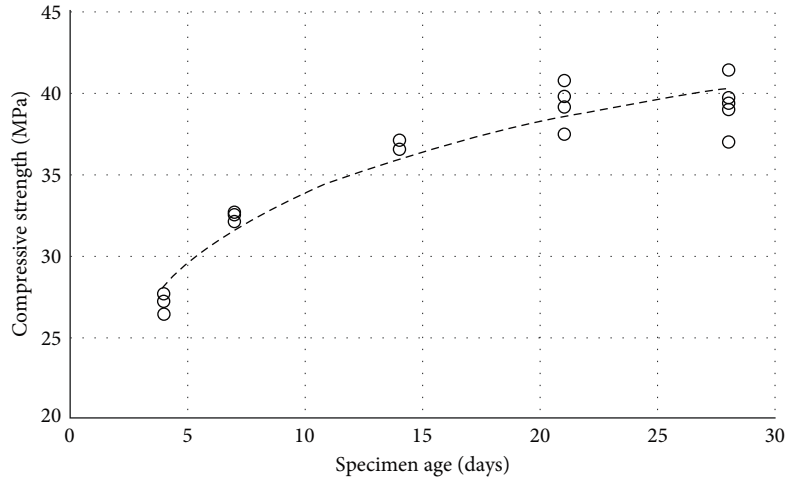

Figure 4: Evolution of unconfined compressive strength (UCS) in concrete specimens cured under ambient conditions (tested according to AS 1012.9).

conditions. One set of prisms was cured and dried according to standard AS 1012.13 [26] (hereafter referred to as "with water curing"). They were cured in water for 7 days and subsequently conditioned in the shrinkage room where moisture and temperature are maintained at standard conditions. The measurement started on the same day as the commencement of drying in the shrinkage room and was measured weekly afterward.

In contrast, the other set of prisms cured in the mould was stored in the same room as the large ring test (hereafter referred to as "ambient drying") for 24 hr, with a plastic sheet covering the top surface to prevent excessive drying. The prisms were still covered with plastic sheets after demolding and only started being fully exposed to the ambient environment simultaneously with the demolding of the large concrete ring. Then, all the prisms were placed next to the large rings with all surfaces exposed to the same environment for the duration of the experiment, and the free shrinkage measurement started concurrently with the start of data acquisition of the ring test.

The free shrinkage of the prisms is depicted in Figure 5. While the free shrinkage measurements of the prisms with water curing offer a standardised index for the shrinkage potential of the concrete used in the experiment, they do not accurately reflect the actual volumetric change of the concrete in the ring test. Compared to the prisms with ambient drying, the drying of the prisms with water curing commenced with a higher water content, and they were conditioned in a shrinkage room where moisture and temperature were maintained at standard conditions, which explains why the prisms processed according to the standard experienced a faster shrinkage rate in the first week and ultimately exhibited more significant shrinkage compared to those subjected to ambient conditions. However, despite sharing the same environment, the free shrinkage measurements of the prisms with ambient drying may not be representative of the free shrinkage of the large concrete ring due to different S_{exp}/V ratios (60 m^{-1} for prisms vs 10 m^{-1} for the large concrete rings).

4.3. Restrained Shrinkage of Concrete Assessed with Large Ring Setup. The calibration coefficient determined in the previous section for each MP has been applied to the original measurements to obtain the corrected net steel strain. The corrected net circumferential strain of Ring A and Ring B over time is shown in Figure 6 (MP1, MP2, MP3) and Figure 7 (MP4, MP5, MP6), respectively, with the negative sign indicating compressive strain. The temperature of the steel rings is also displayed to evaluate the deformation of the ring due to temperature changes.

Overall, all the MPs show a steady increase in compressive strain, with some fluctuations within the first 2 days. The strain changes at the early age are a combined result of temperature changes caused by early-age cement hydration, implied by the temperature curve, which peaked at 31°C and then dropped to the ambient temperature of 20°C. As an

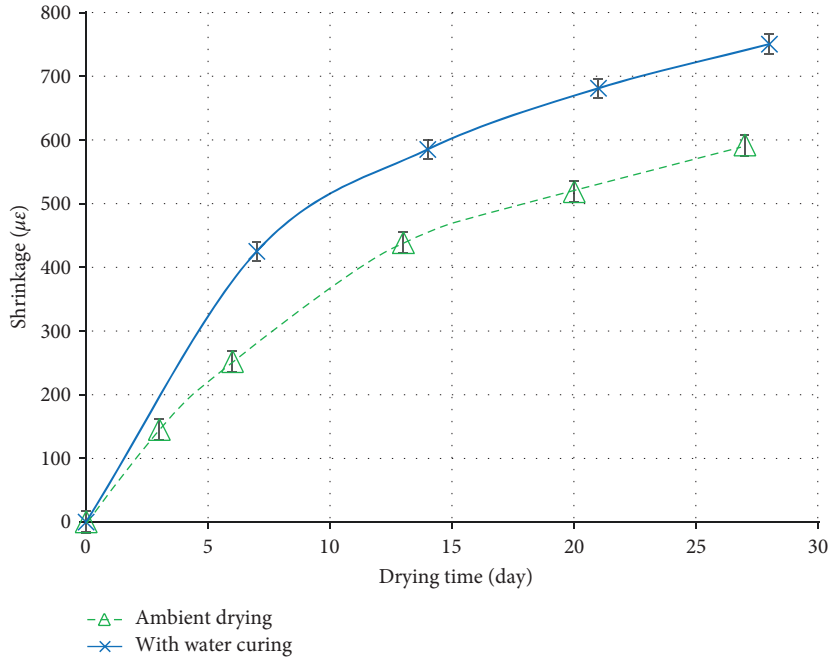

Figure 5: Free shrinkage of the prisms stored alongside the upscaled rings (ambient environment) and standard free shrinkage test (with 7-day water curing).

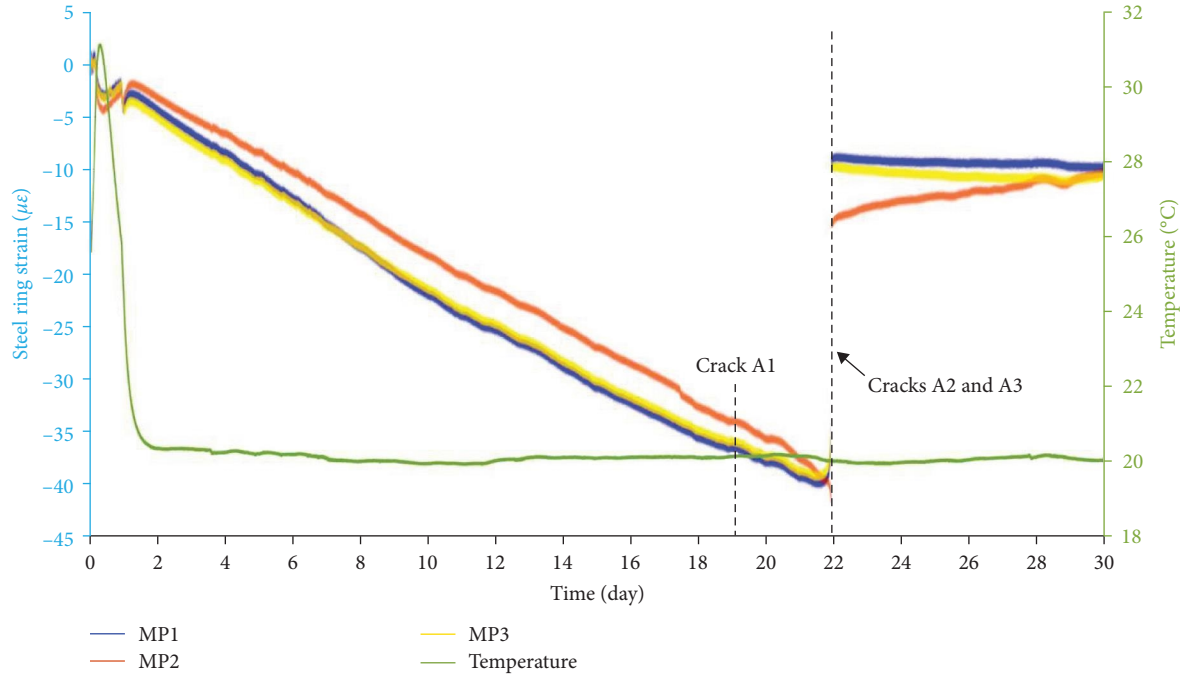

Figure 6: Corrected circumferential strain on the inner surface of Ring A's steel ring, along with the temperature of the steel ring measured using a thermocouple.

example, Figure 8 shows the scatter plot of Ring A strain and temperature at the early age. The concrete temperature increased due to hydration, causing thermal expansion. However, the stiff outer rim as part of the mould was still fixed around the concrete ring, providing additional restraint to the expanding concrete. Thus, the instrumented steel ring underwent contraction from the expanding concrete ring restrained by the outer rim, resulting in a rapid increase in compressive strain in the steel ring. Then, the compressive strain gradually decreased following the decrease in temperature. The subsequent rapid change in steel strain was caused by exposing concrete to the ambient environment after

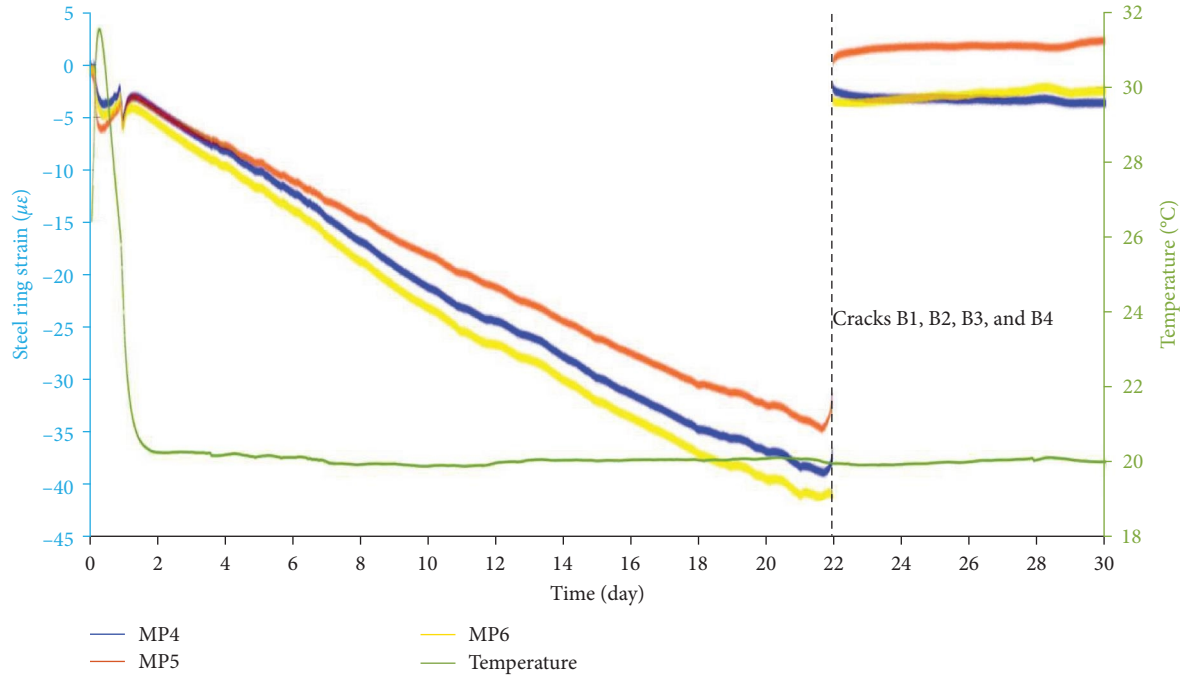

Figure 7: Corrected circumferential strain on the inner surface of Ring B's steel ring, along with the temperature of the steel ring measured using a thermocouple.

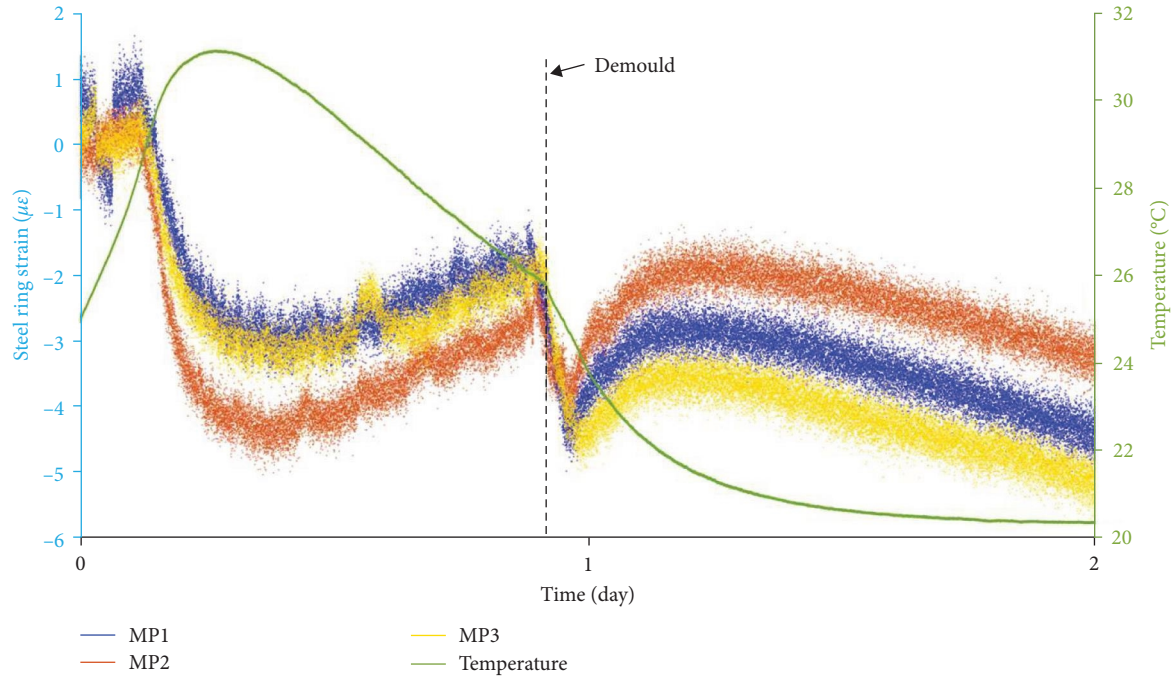

Figure 8: Scatter plot showing corrected circumferential strain on the inner surface of Ring A's steel ring within the first 2 days (12 measurements per minute), along with the temperature of the steel ring measured using a thermocouple.

demolding, with shrinkage due to drying and heat dissipation. Once the steel temperature stabilised at around 20°, all the readings of strain gauges showed a continuous increase in compressive strain until an abrupt change in the strain reading occurred at the age of cracking.

Both Rings A and B exhibited a major crack propagating through the entire thickness of the concrete ring at the age of cracking, corresponding to the date when the sudden change in measured strain occurred. The cracking age was approximately the same for both rings in this experiment, although

Table 6: Characteristic of cracks occurred on concrete rings.

Ring	Crack	Crack width (mm)	Initial crack length (mm)	Final crack length (mm)	Age appeared (day)	Comment
A	A1	<0.1	60	90	19	Not fully propagated
	A2	<0.1	60	60	22	Not fully propagated
	A3	0.7	200	200	22	Top half cracked
	A4	0.7	—	200	39	Bottom half cracked
B	B1	<0.1	55	55	22	Not fully propagated
	B2	<0.1	100	100	22	Not fully propagated
	B3	<0.1	200	200	22	Minor crack
	B4	1	200	200	22	Through full height

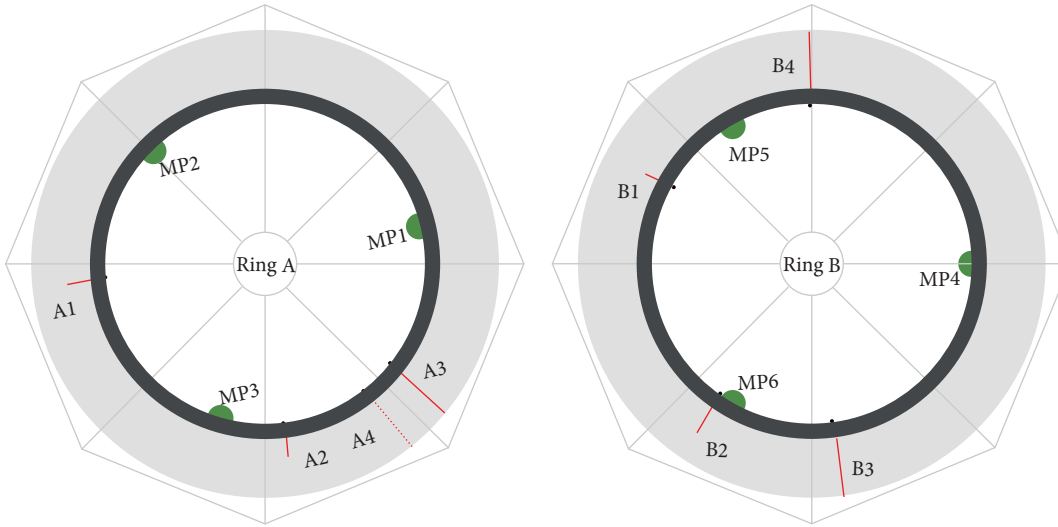

Figure 9: Measured crack patterns on the concrete in Ring A (a) and Ring B (b), with fully propagated macro cracks A3 and B4 indicated with thicker lines.

the residual strain after cracking differed. It is also noteworthy that the cracking age is longer compared to other published experimental data of small ring tests. This discrepancy may be attributed to a smaller S_{exp}/V ratio of the large concrete ring with top and bottom drying (10%) compared to ASTM C1581 (29%) and AASHTO T 34-08 (15%), both of which are under circumferential drying.

Apart from the macro cracks, some micro cracks appeared before or at the age of cracking. However, microcrack propagation ceased before the formation of the macrocrack, and the width and length remained constant until the end of the test. The characteristics of cracks from daily observations are listed in Table 6, and the crack patterns are shown in Figure 9. All the cracks initiated from the steel–concrete interface aligning with the position of the maximum induced stress in pressurised thick-wall cylinders [51]. The crack initiation from the inner circumference of the concrete ring indicates that the impact of differential shrinkage in the radial direction was insignificant with the radial drying setup. In other words, the restraint from the steel ring dominated the crack initiation of the concrete ring.

The formation of multiple cracks may result from the large ring size, with the concrete thickness being thicker than the standardised ring test. It was reported that two major cracks formed at an approximately angular distance of 120° are typically observed in the failure of thick-wall cylinders under internal pressure [27, pp. 29–30]. The angular distance between some cracks formed on the concrete ring in this experiment is close to this value. Besides, no noticeable eccentricity was identified in the two concrete rings, with a measured concrete ring thickness of 200 ± 5 mm for both rings, and none of the observed cracks occurred at the relatively thinner part of the concrete rings. Thus, it is unlikely that the minor irregularity of the concrete ring thickness led to the observed crack pattern.

Moreover, it is apparent from Figure 9 that the macrocracks and some of the micro-cracks occurred near the support arms at the bottom of the concrete ring. Due to the proximity of the cracks to the base support arms, the crack pattern is potentially associated with the tensile stress induced by the deflection of the concrete on the thin steel support arms with its own self-weight. A FE analysis was conducted in ANSYS Workbench to simulate the hoop stress in a concrete ring (density of 2,300 kg m^{-3}) when placed on the support arms (20 mm in width) with the same geometry as the experiment. The highest tensile hoop stress (16 kPa)

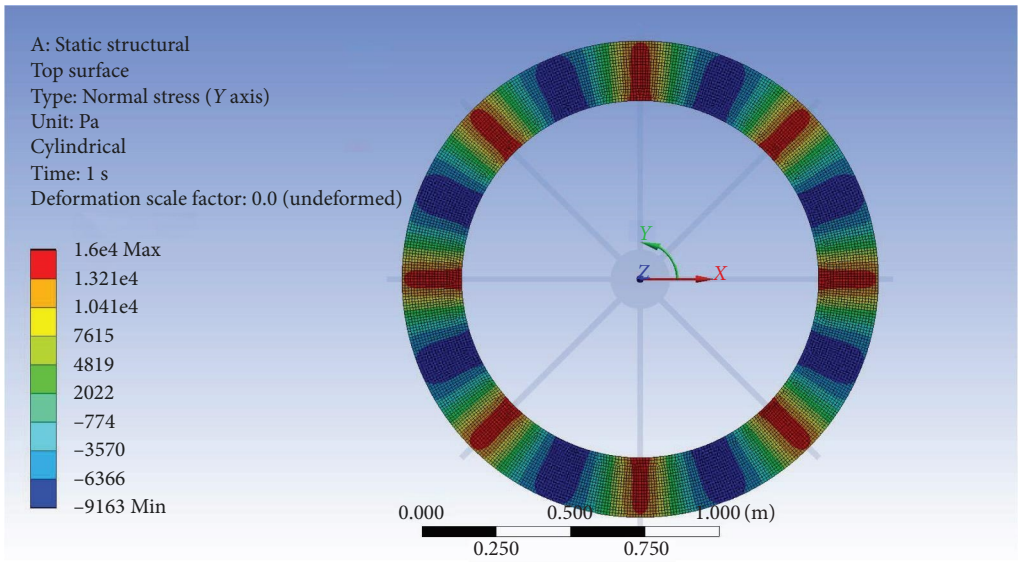

Figure 10: Hoop stress (Pa) on the top surface of the concrete ring (density: 2,300 kg m^{-3}) placed on the support arms.

occurs at the top surface of the portion of the concrete ring right above the steel support arms (Figure 10). This additional tensile stress caused by self-weight might contribute to the initiation of cracks in concrete rings. Therefore, geometry optimisations for both ring specimens and the apparatus are required to minimise the extra tensile stresses.

In the standard ASTM C1581 [29], the cracking potential of different mix designs is compared using the net time-to-cracking and average stress rate based on equations published in [66, 67]. However, the rate of stress development method in ASTM C1581 is based on stress distributions of thin cylinders [44], which is not applicable for the thick concrete ring in this experiment, especially since the drying condition is different from the standardised ring tests. As stated by See et al. [67], it is assumed that in the proposed thin ring test, the concrete ring is subjected to a uniform and uniaxial tensile stress when restrained by the steel ring, as the actual hoop stress on the outer and inner surfaces of the concrete is within 10% of the average stress. This assumption may not be valid for the thick ring tests, and a different geometry constant G [29, 66, 67] should be applied for the calculation of the stress rate of the large ring tests based on the geometry and drying condition.

More importantly, the effect of the unmeasurable restraints and the additional driving force for crack initiation, other than the restraint from the steel ring, should be minimised in the ring test if the stress rate method is used to assess the cracking potential. In the stress rate method, as the strain gauge readings are the primary input for the stress rate method, a direct correlation of the concrete stress with the strain gauge readings can be established if the steel ring is the only restraint that contributes to crack initiation. Further studies on the thick rings' stress rate method are required before extending the stress rate method to assessing the large ring tests.

The maximum induced tensile stress on the thick concrete ring at the age of cracking can be calculated for the thick ring test with the net strain of the steel rings. In this experiential trial, the average maximum net strain of Ring A and Ring B at the age of cracking are 39 and 37 $\mu\varepsilon$, respectively. The induced tensile stress at the inner circumference of the concrete rings at the age of cracking can be estimated with an analytical solution proposed by Hossain and Weiss [68]:

$$\sigma_{\max} = \varepsilon_s(t) \cdot \overline{E}'_S \cdot \frac{R_{OS}^2 + R_{OC}^2}{R_{OC}^2 - R_{OS}^2} \cdot \frac{R_{OS}^2 - R_{IS}^2}{2R_{OS}^2}, \tag{16}$$

where $\varepsilon_s(t)$ is the circumferential strain of the inner surface of the steel ring at a specific age. By applying the average effective modulus $\overline{E}'_S$ to Equation (16) with the maximum net strain, the induced tensile stress at the cracking age can be calculated, which is 2.8 and 2.7 MPa for Rings A and B, respectively. The estimated induced tensile stresses of the rings are slightly lower than the predicted tensile strength (3.3 MPa) at the age of cracking, which indicates that additional driving force may contribute to restrained shrinkage cracking and is not captured by the strain gauge readings.

Apart from the tensile stress induced by the deflection of the concrete on the support arms with its self-weight, the self-restraint caused by the moisture gradient along the height direction is also part of the crack driving force. According to Dong et al. [69], the proportion of the self-restraint caused by the moisture gradient along the height direction in the crack propagation driving force is more significant in taller rings drying from top and bottom surfaces. Given the concrete rings with a height of 200 mm in this experiment, the self-restraint caused by the moisture gradient along the height direction possibly contributed to the crack propagation.

In the large ring test, the friction between concrete and steel arms cannot be negligible due to the weight of the concrete ring (~400 kg). Although two layers of Teflon sheet had been placed between concrete and steel support arms at the bottom of the concrete to reduce friction, the increased

(a) (b)

Figure 11: Crack A3 (occurred on day 22) and Crack A4 (occurred on day 39): (a) isometric view and (b) side view.

weight of the concrete ring and the smaller contact area for support resulted in higher normal stress than the standardised ring tests. Consequently, the resultant friction likely introduced additional restraint to the ring test. Assuming the friction coefficient between concrete and steel is 0.57 [70] without any friction reduction, the resultant static friction at the concrete base can reach up to 71 kPa when the concrete shrinks. It may be a potential cause of the formation of crack A4 on day 39 (Figure 11) near crack A3, as substantial changes in strain gauge readings were observed before and after crack A4 appeared, which implies that the steel ring may not be the restraint initiating crack A4.

5. Conclusion

This paper presents an experimental trial on the large ring test method with cast concrete for potential application in restrained shrinkage cracking of FRS. The instrumentations on the steel ring were tailored for an expected longer test duration, using strain gauges arranged in a full Wheatstone bridge configuration in each MP with temperature compensation and applying thermocouples for steel ring temperature measurement. Additionally, with calibration undertaken on the instrumented steel ring, the effective elastic moduli of the steel rings were estimated using the analytical solution for geometrically thin rings, and calibration coefficients for individual MP were derived for corrections to strain gauge readings. Based on the experimental trial and discussion of the results, the following conclusions can be drawn:

(1) The experiment with cast concrete exhibited a comparable age of cracking and maximum net strain. The results indicate that satisfactory ring specimens can be produced with this setup, and consistent results can be achieved with the instrumentation, calibration, and correction methods proposed in this paper.

(2) The multi-crack formation was observed in the large ring test. The crack initiation from the inner circumference of the concrete ring indicates that the impact of differential shrinkage in the radial direction was insignificant with drying from the top and bottom surfaces.

(3) The outer rim fixed on the outer circumference of the concrete ring before de-moulding was an additional restraint as it restricted the thermal expansion of concrete at the early age, but this restraint was temporary, and the additional compressive strain in the steel ring gradually decreased following the decrease in temperature.

(4) In addition, further studies on the stress rate method for thick ring tests are required, as the ring dimension and the drying condition of this experiment are different from the standardised ring tests. Moreover, the effect of the unmeasurable restraints should be minimised in the ring test if the stress rate method is adapted to assess the cracking potential.

(5) Additional driving forces for crack initiation existed and were not revealed by the strain gauge readings. The potential causes include self-restraint caused by the moisture gradient along the height direction, deflection of the concrete ring caused by self-weight, and increased friction at the contact surface of the support. Therefore, geometry optimisations on both ring specimens and the apparatus are required to minimise the effects of the additional causes for crack initiation other than the restraint from the steel ring.

6. Recommendations for Future Experimental Investigations

Overall, the large ring test results show that using the full Wheatstone bridge and thermocouple ensures that temperature changes are included in the evaluation. However, as the specimens were made with cast concrete instead of sprayed concrete, the effect of the placement position of the moulds and the effect of rebound and spray angle have not been studied. Besides, the effects of rapid changes in stiffness and temperature due to accelerator reactions have not been investigated with the large ring test. Thus, experimental investigation with sprayed shotcrete (accelerated and unaccelerated) is necessary for future experimental studies using large ring tests. A more robust protection for the instruments at the MPs is required if the sprayed concrete is used for specimen production.

Moreover, the effects of the reinforcement fibres have not been examined in this study, especially regarding test duration, multiple cracking, and crack width control. Therefore, large ring tests with fibre-reinforced concrete or shotcrete should be conducted in future research. In addition,

modifications could be made to the free shrinkage test so that the S_{exp}/V ratios of free shrinkage test specimens and large ring test specimens are comparable. In this way, the free shrinkage measured on the small-size specimens can be correlated to the large ring test.

Abbreviations

DOR: Degree of restraint
SG-h: Strain gauge in hoop direction
SG-v: Strain gauge in vertical direction
E_C: Effective elastic modulus of concrete (GPa)
E_S: Elastic modulus of steel (GPa)
E'_S: Effective elastic modulus of steel (GPa)
$\overline{E}_S$: Average effective elastic modulus of steel (GPa)
ε_{C-sh}: Linear free shrinkage of concrete (m m^{-1})
ε_h: Strain caused by external force in the hoop direction (m m^{-1})
ε_S: Strain on the inner surface of the steel ring in the hoop direction (m m^{-1})
ε_T: Strain caused by thermal deformation (m m^{-1})
ε_v: Strain caused by external force in the vertical direction (m m^{-1})
h: Height of steel and concrete ring (m)
k: Strain-gauge factor (unitless)
ν_S: Poisson's ratio of steel (unitless)
ν_C: Poisson's ratio of concrete (unitless)
P: Point load (N)
R_{IS}: Inner radius of the steel ring (m)
R_n: Radius of the neutral surface in thin ring (m)
R_{OC}: Outer radius of the concrete ring (m)
R_{OS}: Outer radius of the steel ring (m)
S_{exp}: Exposed surface area (m^2)
t: Time (s)
U_A: Wheatstone bridge output voltage (V)
U_E: Wheatstone bridge excitation voltage (V)
V: Volume of the specimen or structure (m^3).

Data Availability

The data used in this paper are stored on the Research Data Management site https://rdm.uq.edu.au/. Data will be made available on request.

Conflicts of Interest

The authors declare that they have no conflicts of interest.

Acknowledgments

Zhongyu Xu is the recipient of the Australian Government Research Training Program (RTP) scholarship. This work was performed at the School of Civil Engineering, the University of Queensland, with funding from Dr Jurij Karlovsek's research grant. Open access publishing facilitated by the University of Queensland, as part of the Wiley—the University of Queensland agreement via the Council of Australian University Librarians. The authors would like to acknowledge the support from Aurecon. Acknowledgments also to students involved in the summer research programme for assisting in experiments.

References

[1] Infrastructure Pipeline, "Infrastructure pipeline by project location," 2023, (accessed June 12), https://infrastructurepipeline.org/. https://infrastructurepipeline.org/charts/location-sector.
[2] Victoria's Big Build, "Suburban rail loop," 2023, (accessed June 12), https://bigbuild.vic.gov.au/. https://bigbuild.vic.gov.au/projects/suburban-rail-loop.
[3] Victoria's Big Build, "North east link program," 2023, https://bigbuild.vic.gov.au/projects/north-east-link.
[4] NSW Government, "Western harbour tunnel," 2023, (accessed June 12), https://caportal.com.au/rms/wht.
[5] NSW Government, "Coffs harbour bypass," 2023, (accessed June 12), https://caportal.com.au/rms/coffs.
[6] Australian Rail Track Corporation, "Gowrie to Kagaru project fact sheet," 2023, (accessed June 12), https://inlandrail.artc.com.au/. https://inlandrail.artc.com.au/gowrie-to-kagaru-project-fact-sheet/.
[7] Australian Shotcrete Society, "Shotcreting in Australia: recommended practice," 2020.
[8] T. Collotta, G. Barbieri, and M. Mapelli, "Shotcrete tunnel linings with steel ribs: stress redistribution due to creep and shrinkage effects," in *Shotcrete: Elements of a System*, E. S. Bernard, Ed., pp. 71–84, Taylor and Francis Group, London, England, 2010.
[9] B. Lagerblad, L. Fjällberg, and C. Vogt, "Shrinkage and durability of shotcrete," in *Shotcrete: Elements of a System*, E. S. Bernard, Ed., pp. 173–180, Taylor and Francis Group, London, England, 2010.
[10] A. Thomas, *Sprayed Concrete Lined Tunnels*, CRC Press, London, 2nd edition, 2019.
[11] H. S. Armelin, "*Rebound and Toughening Mechanisms in Steel Fiber Reinforced Dry-Mix Shotcrete*," Doctoral dissertation, University of British Columbia, 1997.
[12] L. Von Rabcewicz, "The new Austrian tunnelling method—part one," *Water Power*, vol. 16, no. 11, pp. 453–457, 1964.
[13] A. Mueller, "Pacific highway upgrade from Tintenbar to Ewingsdale (T2E), St Helena tunnel," in *15th Australasian Tunnelling Conference 2014: Underground Space-Solutions for the Future*, Engineers Australia and Australasian Institute of Mining and Metallurgy, 2014.
[14] P. Clark, M. Burke, and R. Khatri, "Durability of steel fibre reinforced shotcrete-a review of published technical papers, codes and standards," in *Paper presented at the 16th Australasian Tunnelling Conference*, Sydney, 2017.
[15] A. Ansell, "Investigation of shrinkage cracking in shotcrete on tunnel drains," *Tunnelling and Underground Space Technology*, vol. 25, no. 5, pp. 607–613, 2010.
[16] A. M. Neville, *Properties of Concrete*, Prentice Hall, Parson Education, Harlow, England, 4th edition, 2002.
[17] K. Kovler and S. Zhutovsky, "Overview and future trends of shrinkage research," *Materials and Structures*, vol. 39, no. 9, pp. 827–847, 2006.
[18] E.-I. Tazawa, *Autogenous Shrinkage of Concrete*, CRC Press, Florida, United States of America, 2019.
[19] H. Ye and A. Radlińska, "A review and comparative study of existing shrinkage prediction models for portland and non-portland cementitious materials," *Advances in Materials Science and Engineering*, vol. 2016, Article ID 2418219, 13 pages, 2016.

[20] European Committee for Standardization (CEN), "EN 1992-1-1 Eurocode 2: design of concrete structures," 2014.
[21] European Committee for Standardization (CEN), "EN 1992-2 Eurocode 2: design of concrete structures," 2008.
[22] V. Gribniak, G. Kaklauskas, R. Kliukas, and R. Jakubovskis, "Shrinkage effect on short-term deformation behavior of reinforced concrete—when it should not be neglected," *Materials & Design*, vol. 51, pp. 1060–1070, 2013.
[23] E. S. Bernard and A. H. Thomas, "Fibre reinforced sprayed concrete for ground support," *Tunnelling and Underground Space Technology*, vol. 99, Article ID 103302, 2020.
[24] S. Altoubat, M. Talha Junaid, M. Leblouba, and D. Badran, "Effectiveness of fly ash on the restrained shrinkage cracking resistance of self-compacting concrete," *Cement and Concrete Composites*, vol. 79, pp. 9–20, 2017.
[25] W. J. Weiss, W. Yang, and S. P. Shah, "Influence of specimen size/geometry on shrinkage cracking of rings," *Journal of Engineering Mechanics*, vol. 126, no. 1, pp. 93–101, 2000.
[26] Standards Australia, "AS 1012.13. 2015: methods of testing concrete: determination of the drying shrinkage of the concrete samples prepared in the field or in the laboratory," 2015.
[27] J. Carlswärd, "*Shrinkage cracking of steel fibre reinforced self compacting concrete overlays: test methods and theoretical modelling: test methods and theoretical modelling*," Doctoral dissertation, Luleå tekniska universitet, Luleå, 2006.
[28] K. Noghabai, "*Effect of tension softening on the performance of concrete structures: experimental, analytical and computational studies*," Doctoral dissertation, Luleå tekniska universitet, Luleå, 1998.
[29] ASTM International, "ASTM C1581/C1581M-18a standard test method for determining age at cracking and induced tensile stress characteristics of mortar and concrete under restrained shrinkage," 2018.
[30] American Association of State Highway and Transportation Officials, "AASHTO 334-08 standard method of test for estimating the cracking tendency of concrete," 2008.
[31] K. Raoufi, E. S. Bernard, and W. J. Weiss, "Shrinkage cracking behavior of fiber reinforced concrete: as assessed using the restrained ring test," *Journal of ASTM International*, vol. 7, no. 7, pp. 1–15, 2010.
[32] J. Kaufmann, K. Frech, P. Schuetz, and B. Münch, "Rebound and orientation of fibers in wet sprayed concrete applications," *Construction and Building Materials*, vol. 49, pp. 15–22, 2013.
[33] P. Pujadas, A. Blanco, S. Cavalaro, A. de la Fuente, and A. Aguado, "Fibre distribution in macro-plastic fibre reinforced concrete slab-panels," *Construction and Building Materials*, vol. 64, pp. 496–503, 2014.
[34] M. Manca, "*The effects of fibre distribution on the performance of fibre-reinforced concrete and shotcrete*," Doctoral dissertation, The University of Western Australia, 2018.
[35] A. Gagnon and W. Geers, *Fiber-Reinforced Shotcrete-Applications and Testing Overview*, Shotcrete Magazine, 2019.
[36] E. Bernard, G. Xu, and N. Carino, *Precision of the ASTM C1550 Panel Test and Field Variation in Measured FRS Performance*, Taylor & Francis, London, 2010.
[37] E. S. Bernard, "Correlations in the behaviour of fibre reinforced shotcrete beam and panel specimens," *Materials and Structures*, vol. 35, pp. 156–164, 2002.
[38] S. Girard, M. Jolin, B. Bissonnette, and J.-D. Lemay, "Measuring the cracking potential of shotcrete," *Concrete International*, vol. 39, no. 8, pp. 44–48, 2017.
[39] B. Menu, A. Pepin Beaudet, M. Jolin, and B. Bissonnette, "Experimental study on the effect of key mix design parameters on shrinkage and cracking resistance of dry-mix shotcrete," *Construction and Building Materials*, vol. 320, Article ID 126216, 2022.
[40] BOSFA, "Applications-shotcrete," 2023, https://bosfa.com/applications/shotcrete/.
[41] S. Australia, "Fibers," 2023, https://aus.sika.com/en/construction/concrete/fibres.html.
[42] Barchip, "Products," 2023, https://barchip.com/product/.
[43] Z. P. Bazant and J. Planas, *Fracture and Size Effect in Concrete and Other Quasibrittle Materials*, CRC Press, Boca Raton, 1998.
[44] F. Kanavaris, M. Azenha, M. Soutsos, and K. Kovler, "Assessment of behaviour and cracking susceptibility of cementitious systems under restrained conditions through ring tests: a critical review," *Cement and Concrete Composites*, vol. 95, pp. 137–153, 2019.
[45] J. H. Moon, *Shrinkage, residual stress, and cracking in heterogeneous materials*, Doctoral dissertation, Purdue University, 2006.
[46] J.-H. Moon, F. Rajabipour, B. Pease, and J. Weiss, "Quantifying the influence of specimen geometry on the results of the restrained ring test," *Journal of ASTM International*, vol. 3, no. 8, pp. 1–14, 2006.
[47] D. Shen, H. Shi, X. Tang, Y. Ji, and G. Jiang, "Effect of internal curing with super absorbent polymers on residual stress development and stress relaxation in restrained concrete ring specimens," *Construction and Building Materials*, vol. 120, pp. 309–320, 2016.
[48] W. Dong, X. Zhou, Z. Wu, and G. Kastiukas, "Effects of specimen size on assessment of shrinkage cracking of concrete via elliptical rings: thin vs. thick," *Computers & Structures*, vol. 174, pp. 66–78, 2016.
[49] O. G. Oladiran, *Assessment of restrained shrinkage cracking of concrete through elliptical rings*, Doctoral dissertation, Brunel University, 2014.
[50] W. Dong, X. Zhou, and Z. Wu, "A fracture mechanics-based method for prediction of cracking of circular and elliptical concrete rings under restrained shrinkage," *Engineering Fracture Mechanics*, vol. 131, pp. 687–701, 2014.
[51] A. B. Hossain and J. Weiss, "The role of specimen geometry and boundary conditions on stress development and cracking in the restrained ring test," *Cement and Concrete Research*, vol. 36, no. 1, pp. 189–199, 2006.
[52] J. Hogancamp and Z. Grasley, "The use of microfine cement to enhance the efficacy of carbon nanofibers with respect to drying shrinkage crack resistance of portland cement mortars," *Cement and Concrete Composites*, vol. 83, pp. 405–414, 2017.
[53] K. Hoffmann, *Applying the Wheatstone Bridge Circuit*, HBM Germany, 1974.
[54] R. N. Swamy, A. K. Bandyopadhyay, and H. Stavrides, "The ring method of measuring restrained shrinkage in mortar and concrete," *Cement, Concrete and Aggregates*, vol. 1, no. 1, pp. 13–20, 1979.
[55] A. Zieliński and M. Kaszyńska, "Calibration of steel rings for the measurement of strain and shrinkage stress for cement-based composites," *Materials*, vol. 13, no. 13, Article ID 2963, 2020.
[56] S. Timoshenko, *Strength of Materials, Part II. Advanced Theory and Problems*, Vol. 245, New York, NY, USA, Van Nostrand, 2nd edition, 1955.
[57] S. Timoshenko, *Strength of Materials Part I. Elementary Theory and Problems*, D. Van Nostrand, New York, NY, USA, 1955.
[58] Hanson Australia, "Concrete products designed to be sprayed on sloping, vertical & overhead surfaces," https://www.hanson.com.au/products/concrete/sprays/.

[59] D. G. Flom and N. T. Porile, "Friction of teflon sliding on teflon," *Journal of Applied Physics*, vol. 26, no. 9, pp. 1088–1092, 1955.
[60] H. Zhu, H.-R. Li, and X.-C. Zhu, "On concrete restrained eccentric ring and squared eccentric ring shrinkage test methods," *Construction and Building Materials*, vol. 84, pp. 239–244, 2015.
[61] Standards Australia, "AS 1012.9: 2014: methods of testing concrete: compressive strength tests-concrete, mortar and grout specimens," 2014.
[62] Standards Australia, "AS 1012.17-1997: methods of testing concrete: determination of the static chord modulus of elasticity and Poisson's ratio," 1997.
[63] Standards Australia, "AS 1012.10-2000: methods of testing concrete: determination of indirect tensile strength of concrete cylinders ('Brazil' or splitting test)," 2000.
[64] Standards Australia, "AS 1012.11-2000: method of testing concrete determination of the modulus of rupture: determination of the modulus of rupture," 2000.
[65] Standards Australia, "AS 3600: 2018 concrete structures," 2018.
[66] H. T. See, E. K. Attiogbe, and M. A. Miltenberger, "Potential for restrained shrinkage cracking of concrete and mortar," *Cement, Concrete & Aggregates*, vol. 26, no. 2, pp. 1–8, 2004.
[67] H. T. See, E. K. Attiogbe, and M. A. Miltenberger, "Shrinkage cracking characteristics of concrete using ring specimens," *Materials Journal*, vol. 100, no. 3, pp. 239–245, 2003.
[68] A. B. Hossain and J. Weiss, "Assessing residual stress development and stress relaxation in restrained concrete ring specimens," *Cement and Concrete Composites*, vol. 26, no. 5, pp. 531–540, 2004.
[69] W. Dong, W. Yuan, X. Zhou, and F. Wang, "The fracture mechanism of circular/elliptical concrete rings under restrained shrinkage and drying from top and bottom surfaces," *Engineering Fracture Mechanics*, vol. 189, pp. 148–163, 2018.
[70] B. G. Rabbat and H. G. Russell, "Friction coefficient of steel on concrete or grout," *Journal of Structural Engineering*, vol. 111, no. 3, pp. 505–515, 1985.